Research Article

# Solution of Stress Intensity Factor and Its Sensitivity Analysis of Notched Semi-circular Bend Specimens

**Long Cheng[1], Shuren Wang[1, 2*], Lizhen Qian[3], and Sen Liu[1]**

[1]*International Joint Research Laboratory of Henan Province for Underground Space Development and Disaster Prevention, Henan Polytechnic University, Jiaozuo 454003, China*
[2]*Collaborative Innovation Center of Coal Work Safety and Clean High Efficiency Utilization, Henan Polytechnic University, Jiaozuo 454003, China*
[3]*China Construction Fifth Engineering Bureau the Third Construction Co., Ltd., Changsha 410004, China*

___

### Abstract

To explore the solution of the dynamic stress intensity factor (SIF) of the fracture model I, static and dynamic three-point bending numerical tests on the notched semi-circular bend (NSCB) specimens were conducted by using Abaqus software. The method of dimensional analysis was used to fit the *K*-factor formula of the fracture model I under static loading. Then this expression was extended to solve for the stress intensity factor under dynamic loading. The SIF was analyzed with the relative crack length *a/R* (*a* is the crack length, *R* is the radius of the specimen) and *S/R* (*2S* is the simply supported distance of the specimen) under static loading conditions, and the effects of the stress pulse duration and wave shape on achieving dynamic force equilibrium were analyzed under dynamic loading. Results show that the static SIF increase with the increase of *a/R* and *S/R*, and the triangular stress pulses during 200 μs, 300 μs and 400 μs have similar trends with the trapezoidal stress pulses in achieving stress uniformity in the specimens. When the dynamic equilibrium is achieved under dynamic loading, the curve of dynamic SIF with time derived from the static *K*-factor formula has a smaller error compared with the results obtained by the dynamic finite element method. The conclusions obtained provide a significantly reference for the fracture analysis.

*Keywords:* Three-point bending test, Stress intensity factor, Stress pulse, Finite element method

___

## 1. Introduction

In the tunnel construction and deep mining, the rock being excavated be often subjected to the external impact loads [1-3]. In addition, due to the large number of cracks, joints, pore spaces and other defects in the natural rock mass, the impacted rock mass exhibits different dynamic fracture characteristics [4-6]. The damaged rock mass during the excavation in engineering not only increases the cost of the later grouted rock bolting, but also causes a decrease in rock stability and even leads to the engineering accidents such as the collapse of the driving face [7, 8].

The large stress gradients under loading are generated at the crack tip in a structural body, and the strength criterion based on the assumption of uniform continuity is no longer applicable. The stress intensity factor (SIF), an important parameter for the material fracture in fracture mechanics, controls the stress and displacement fields near the crack tip and provides an important basis for predicting the initiation and development of the crack [9, 10]. Now many scholars have studied the dynamic fracture behavior of the medium containing crack defects, and the study of static SIF has been relatively well established, but the solution of the dynamic SIF under dynamic loading has rarely been reported.

As an important parameter in fracture mechanics, the SIF is directly related to the extension of cracks in the material. In particular, the dynamic SIF is more widely used

in the engineering practice. Therefore, it is of great significance to study the dynamic SIF under impact loading for the related research and engineering.

## 2. State of the art

At present, the research on the static SIF has been well studied. Regarding the testing method, the International Society for Rock Mechanics (ISRM) has proposed four types of specimens to test the mode I fracture toughness of rocks, namely chevron notched short rod (SR) specimen, chevron notched three-point bend round bar (CB) specimen, cracked chevron notched Brazilian disc (CCNBD) specimen, and notched semi-circular bend (NSCB) specimen [11-13]. In addition to the four configurations recommended by ISRM, a number of other configurations have been proposed to test the fracture toughness of rock materials in pure mode I, II, III or mixed modes [14, 15]. One of the NSCB specimen proposed by Chong and Kuruppu was adopted by ISRM in 2014 for static fracture toughness tests, and it has been widely used for fracture toughness tests due to its simple structure, easy to preparation and loading [16]. Mirsayar et al. made an NSCB specimen by using asphalt concrete and port-land cement concrete to obtain fracture toughness for different mix mold conditions and to derive a fracture criterion for the test bond section [17]. Fayed evaluated the fracture properties of NSCB specimens using an in-house finite element code and found that SIF of mode I decreases with increasing crack angle or decreasing the span

length [18]. Tang et al. carried out the edge-cracked semicircular bend (SCB) tests on sand rock samples with different moisture contents, and they found that SIF of mode I decreased linearly with increasing moisture content in all specimens with different notch angles [19].

In terms of dynamic loading, based on cracked straight through flattened Brazilian disc (CSTFBD) subjected to split Hopkinson pressure bar (SHPB) impact loading, Wang et al. applied experimental-numerical-analytical methods to study the dynamic crack initiation and extensional toughness of types I and II of rocks [20, 21]. Based on a single cleavage semicircle compression specimen, Wang et al. carried out a dynamic fracture test study of mixed type I/II rock using SHPB, and they found that the crack extension rate was not a constant and maight stop briefly during extension [22]. Furthermore, Wang et al. conducted the related experiments also [23]. The mixed-mode I/II crack often transforms from this mode to the pure mode I during crack propagation, and several velocity decelerations often induce the crack deflection. Virgo et al. investigated the relationship between different crack propagation rates and dynamic SIFs based on the strain gauge method and photoelastic coating method respectively, and they derived the dynamic fracture toughness [24, 25]. Johdon et al. analyzed the continuous changes in crack tip velocity and strain field based on dynamic three-point bending loading tests using the strain gauge method [26].

Although many scholars have conducted lots of studies on different types of crack propagation in terms of SIFs, especially the solution of SIFs under static conditions, there is still a lack of in-depth research on the factors affecting the sensitivity of dynamic SIFs. In this study, by carrying out numerical simulations of model I fracture on NSCB configuration specimens, the static SIF equation was fitted based on the numerical simulation results and extended to solve the dynamic SIF under static loading conditions. The results showed a small error between the calculated and simulated results.

The rest of this study is organized as follows. Section 3 is determination of the equation for the static SIF *K*. Section 4 gives the results of sensitivity analysis of dynamic SIFs, and finally, the conclusions are summarized in Section 5.

## 3. Methodology

### 3.1 Finite Element Model

The schematic diagrams and finite element models of the pure type I under the static and dynamic loading of the NSCB specimens are shown in Figs. 1 and 2, respectively [27]. The parameters of NSCB specimen geometry model is as following: the radius *R* is 50 mm, the thickness *B* is 20 mm, *a* represents the crack length, the simply supported distance is 2*S*, and the relative crack length $a/R$ is 0.1, 0.2, 0.3, 0.4, 0.5, 0.6, 0.7, and 0.8; $S/R$ is 0.3, 0.4, 0.5, 0.6, 0.7, and 0.8. The radius of the incident bar and transmission bar is 50 mm, and the Poisson's length *l* is 2050 mm.

The elasticity modulus *E* of the specimens is 30 GPa, the Poisson's ratio $\mu$ is 0.2, and the density $\rho$ is 2500 kg/m³. The elasticity modulus of the incident bar and transmission bar is 210 GPa, the Poisson's ratio $\mu$ is 0.3, and its density $\rho$ is 7850 kg/m³.

Due to the symmetry of the SHPB loading model, in order to improve the calculation efficiency, the overall 1/4 model was established, except for the crack tip of the specimen where C3D6 units were used, the rest and the

incident and transmission bars were used C3D8R units. The static model CPS6 units were used at the crack tip and CPS8 units for the rest.
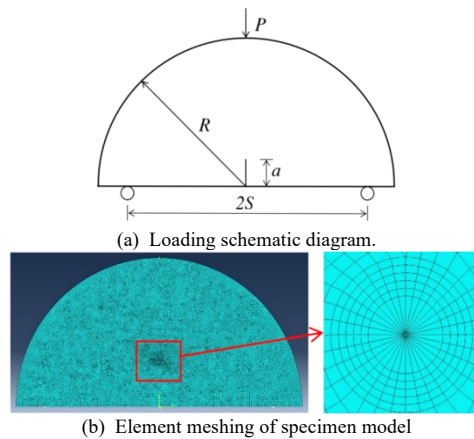


(a) Loading schematic diagram.



(b) Element meshing of specimen model

**Fig. 1.** Finite element model under static loading.



(a) Loading schematic diagram of SHPB
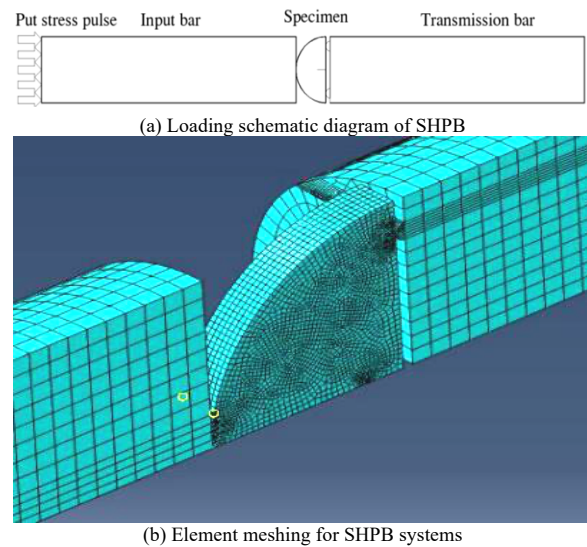


(b) Element meshing for SHPB systems

**Fig. 2.** Finite element model under dynamic loading.

### 3.2 Equation for the stress intensity factor *K*

Using the method of dimensional analysis and the equations in reference [13], the NSCB specimens were denoted as:

$$K_{\mathrm{I}} = \frac{P\sqrt{\pi a}}{2RB} Y_{\mathrm{I}}\left(\frac{a}{R}, \frac{S}{R}\right) \tag{1}$$

where $Y_{\mathrm{I}}$ is the non-dimensional stress intensity factor, only related to the geometric configuration of the specimen.

For the next analysis, Eq. (1) can be transformed as:

$$Y_{\mathrm{I}}\left(\frac{a}{R}, \frac{S}{R}\right) = \frac{2K_{\mathrm{I}} RB}{P\sqrt{\pi a}} \tag{2}$$

### 3.3 Some assumptions of SHPB system

The working principle of SHPB system satisfies two basic assumptions [28], one is the one-dimension stress wave assumption, that is, the stress wave propagates in the elastic bar with a horizontal section of the bar and the axial stress in the horizontal section is uniformly distributed along the radius direction. The second is the stress homogenization assumption, that is, the stress difference between the two ends of the specimen is small and tends to be in stress equilibrium. The presence of the transverse inertia effect

during dynamic loading that causes the stress waves to spread out during propagation, resulting in the phenomenon of wave dispersion. When the wave dispersion is evident, it can homogenize the stress wave propagation and the stress in the specimen, which can have an impact on the accuracy of the test results. In the test, the pulse shaping technique is used to improve the loading waveform.

Considering transverse kinetic energy, the expression for the axial stress in the compression bar is [29].

$$\sigma = E\varepsilon + \rho_0 v^2 r_g^2 \frac{\partial^2 \varepsilon}{\partial t^2} \tag{3}$$

where $v$ is the Poisson's ratio. $r_g$ is the radius of gyration of the section on the $x$-axis.

Due to the transverse inertia, the Rayleigh approximation to the harmonic wave-speed can be written as:

$$\frac{C}{C_0} \approx 1 - v^2 \pi^2 \left(\frac{r}{\lambda}\right)^2 \tag{4}$$

where $r$ is the radius of the compression member. $\lambda$ is the wavelength, and $C_0$ is the one-dimension stress wave speed.

## 4. Results analysis and discussion

### 4.1 Analysis of $Y_I$ with $a/R$ and $S/R$

The 48 models were bulit by Abaqus with $a/R=0.1$-$0.8$ and $S/R=0.3$-$0.8$ to calculate the SIF-$K_I$. $Y_I$ can be calculated by the Eq. (2).

As seen from Figs. 3 and 4, when $S/R$ is certain, $K_I$ and $Y_I$ change consistently, both show a good exponential growth with the increase of $a/R$. When $a/R$ is certain, $K_I$ and $Y_I$ show a linear growth with the increase of $S/R$, and the linear growth rate is faster when the relative crack length $a/R$ is greater than 0.5. The closer the crack tip is to the loading point, the more concentrated the crack tip vertical crack plane tensile stress is, the crack tip stress intensity factor tends to increase, and the increase of $S/R$ has a certain enhancement effect on the SIF of the crack tip.
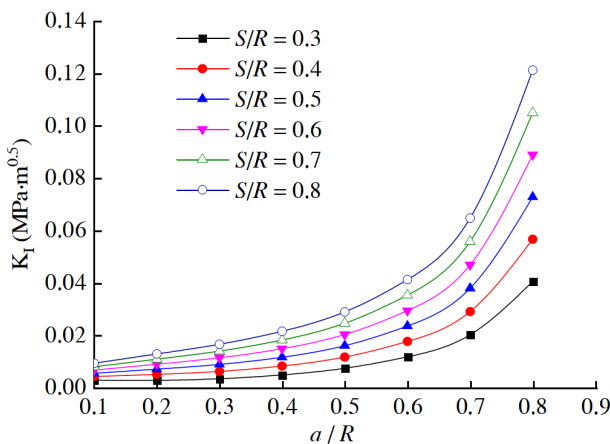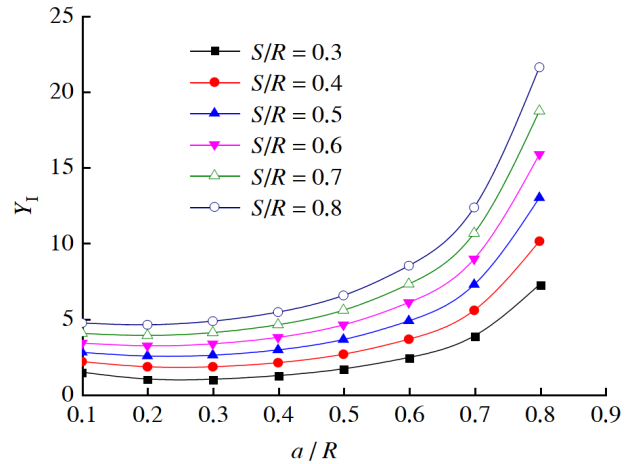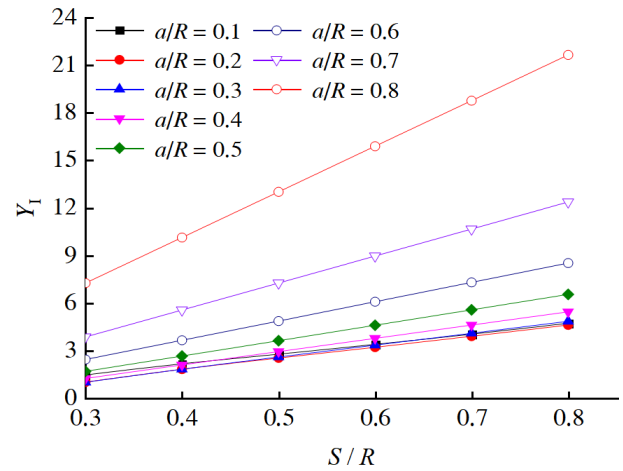


(a) Curves variation between $K_I$ and $a/R$
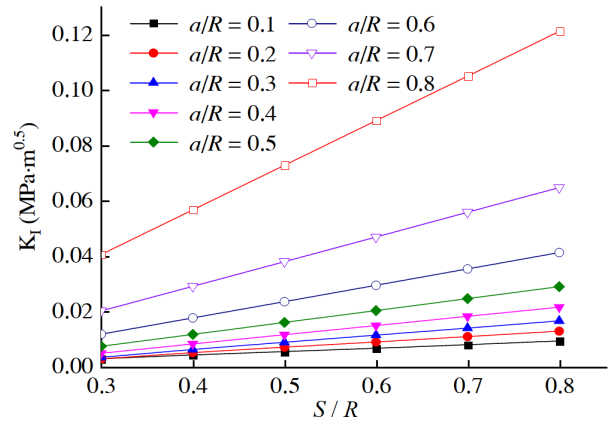


(b) Curves variation between $K_I$ and $S/R$

**Fig. 3.** Curves variation of $K_I$ with $a/R$ and $S/R$.



(a) Curves variation between $Y_I$ and $a/R$



(b) The relationship between $Y_I$ and $S/R$

**Fig. 4.** Curves variation of $Y_I$ with $a/R$ and $S/R$.

Then, $Y_I$ satisfies the following exponential growth Eq. (5):

$$Y_I\left(\frac{a}{R}, \frac{S}{R}\right) = y + A\, e^{\frac{a/R}{t}} \tag{5}$$

The $Y_I$ is also determined by the coefficients $y$, $A$ and $t$. For different $S/R$, the corresponding coefficients $y$, $A$ and $t$ are different, as shown in Table 1.

**Table 1.** $S/R$ related to the coefficients $y$, $A$ and $t$.

| $S/R$ | 0.3 | 0.4 | 0.5 | 0.6 | 0.7 | 0.8 |
|-------|-----|-----|-----|-----|-----|-----|
| $y$ | 1.077 | 1.835 | 2.515 | 3.178 | 3.852 | 4.552 |
| $A$ | 0.011 | 0.015 | 0.021 | 0.029 | 0.036 | 0.042 |
| $t$ | 0.126 | 0.126 | 0.129 | 0.131 | 0.133 | 0.133 |

It can be seen from Eqs. (1) and (2), the accuracy of the SIF-$K$ also depends on $Y_1$, and $Y_1$ depends on the coefficients $y$, $A$ and $t$. Therefore, the values of $y$, $A$ and $t$ in Table 1 are fitted to the equation with $S/R$ respectively, and the results are as follows:
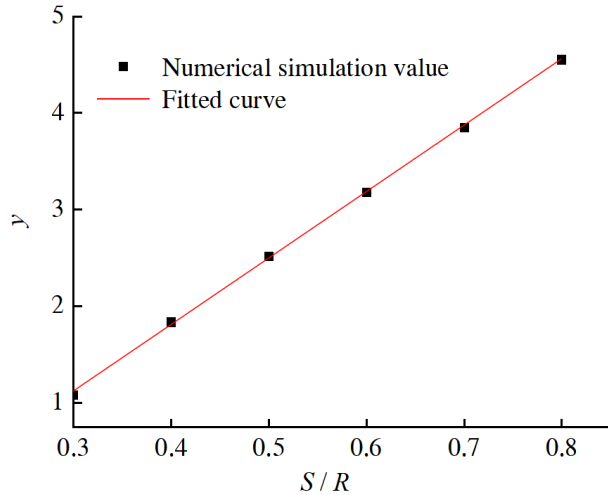


(a) Fitted curve for $y$
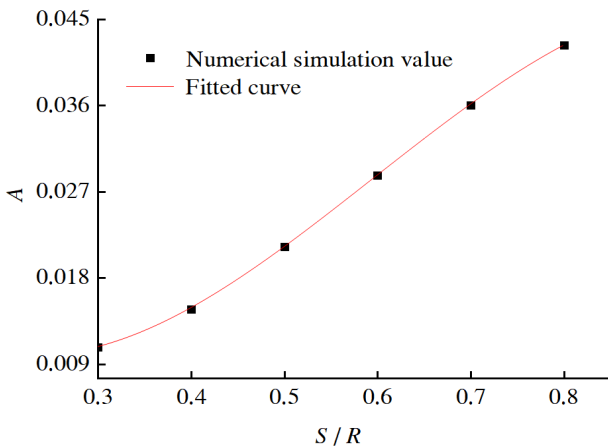


(b) Fitted curve for $A$
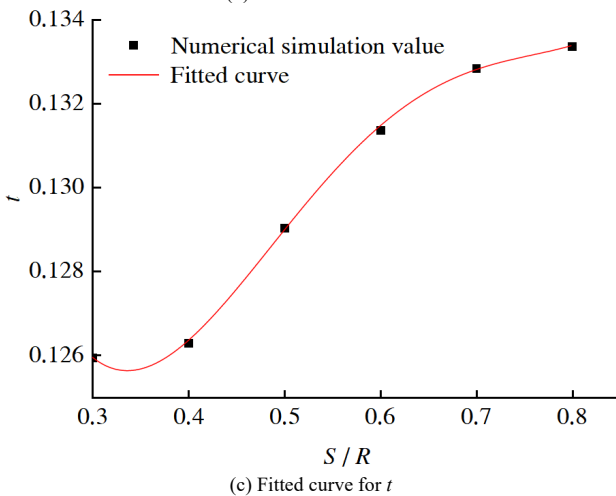


(c) Fitted curve for $t$

**Fig. 5.** Curves variation of $Y_I$ with coefficients $y$, $A$ and $t$.

As seen from Fig. 5, the fitted curves for $y$, $A$ and $t$ have a high accuracy, and the equation can be obtained as:

$$y = a\left(\frac{S}{R}\right) + b \tag{6}$$

where $a$ is 6.882 and $b$ is -0.950. The correlation coefficient is 0.997.

$$A = B_0 + B_1\left(\frac{S}{R}\right) + B_2\left(\frac{S}{R}\right)^2 + B_3\left(\frac{S}{R}\right)^3 \tag{7}$$

where $B_0$ is 0.024, $B_1$ is -0.132, $B_2$ is 0.351, and $B_3$ is -0.197. The correlation coefficient is 0.999.

$$t = C_0 + C_1\left(\frac{S}{R}\right) + C_2\left(\frac{S}{R}\right)^2 + C_3\left(\frac{S}{R}\right)^3 + C_4\left(\frac{S}{R}\right)^4 \tag{8}$$

where coefficients $C_0$ is 0.182, $C_1$ is -0.455, $C_2$ is 1.265, $C_3$ is -1.423 and $C_4$ is 0.571. The correlation coefficient is 0.998.

As seen from Fig. 6, the curves basically cross each simulated value and the fitted formula has a high accuracy. So, the static formula is ready for application to the dynamic analysis.
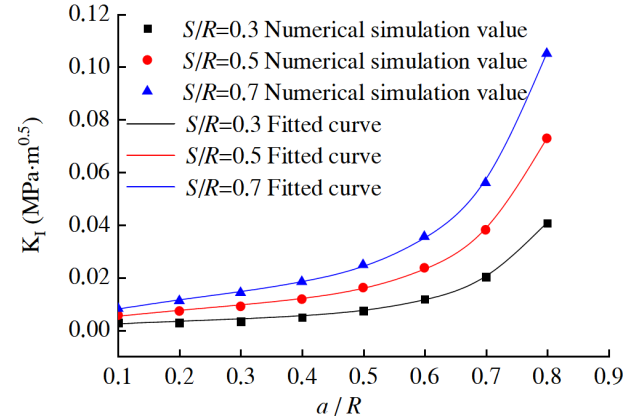


**Fig. 6.** Curves variation of $K_I$ with $a/R$.

**4.2 Stress pulses and verification of dynamic force equilibrium**

The trapezoidal and triangular pulses during 200 μs, 300 μs and 400 μs were applied to the incident bar end part for the established 1/4 SHPB loading system, and the contact forces between the specimen and the incident bar and the transmission bar were extracted from the left and right sides, and the equilibrium of the contact forces between the left and right sides was compared to determine the more suitable stress pulse. The loading waveforms are shown in Fig. 7.
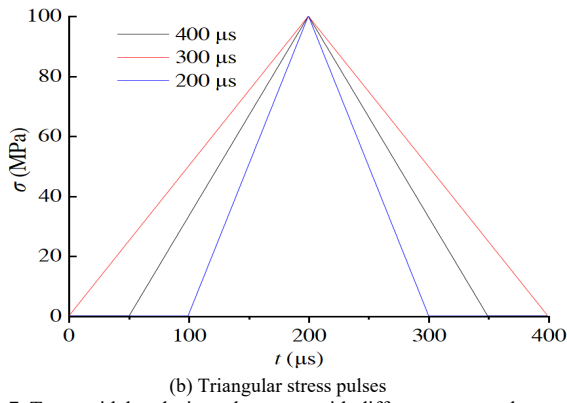


(a) Trapezoidal stress pulse
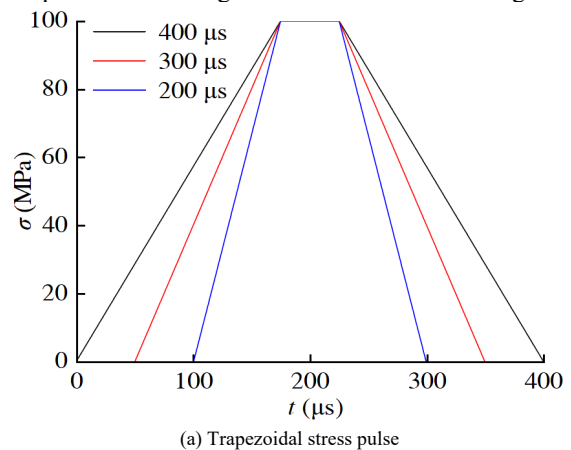
(b) Triangular stress pulses

**Fig. 7.** Trapezoidal and triangular stress with different stress pulses.

The calculated results of the specimen model with $a/R=0.2$ and $S/R=0.8$ are selected and the contact forces extracted from the left and right sides of the specimen are shown in Figs. 8 and 9.
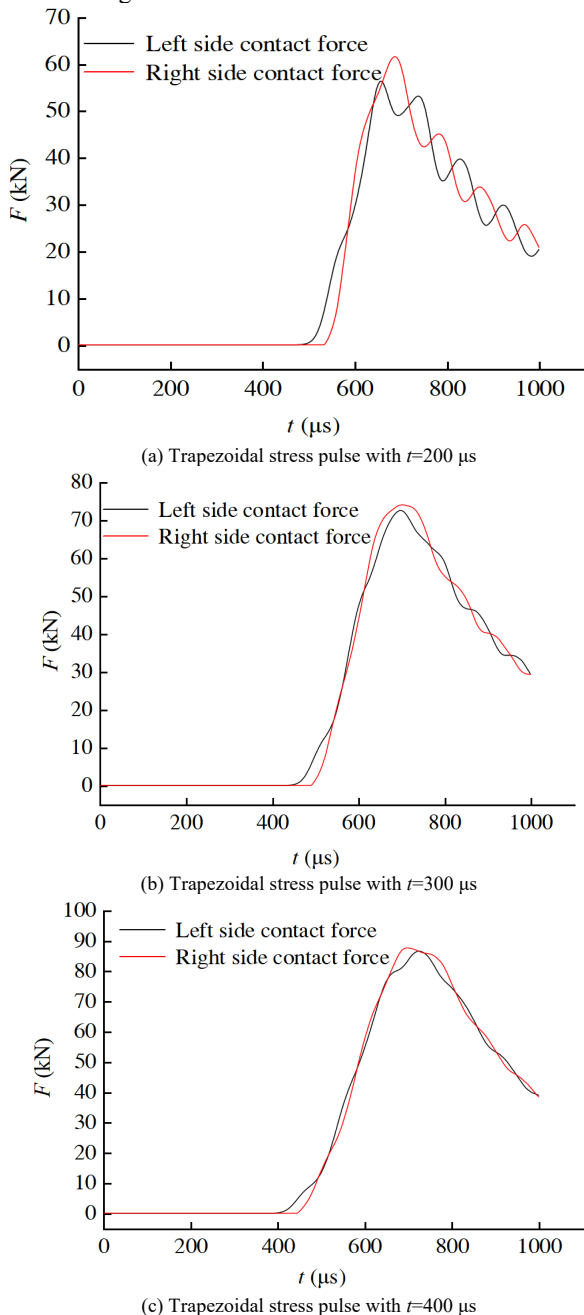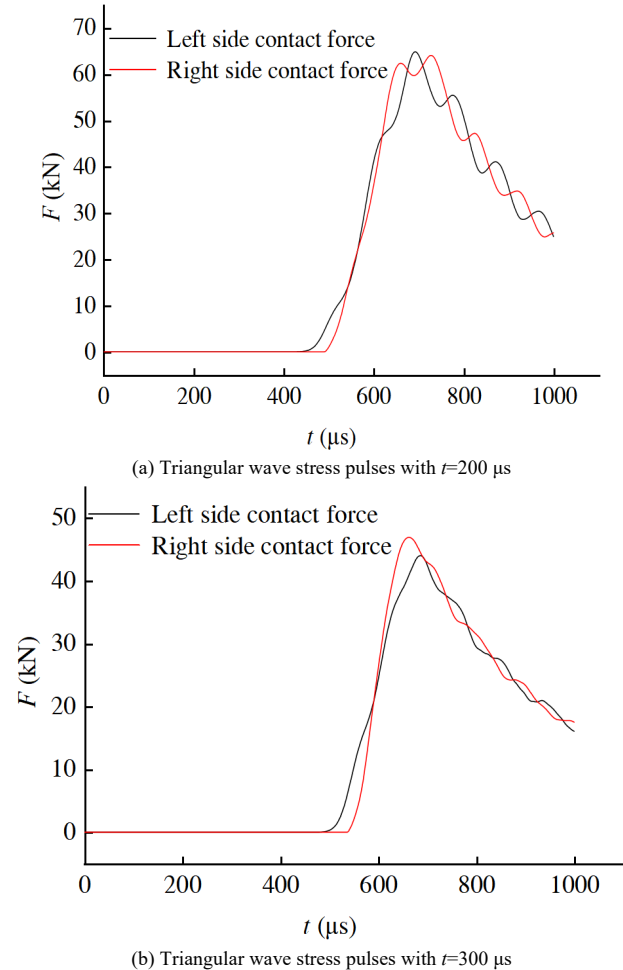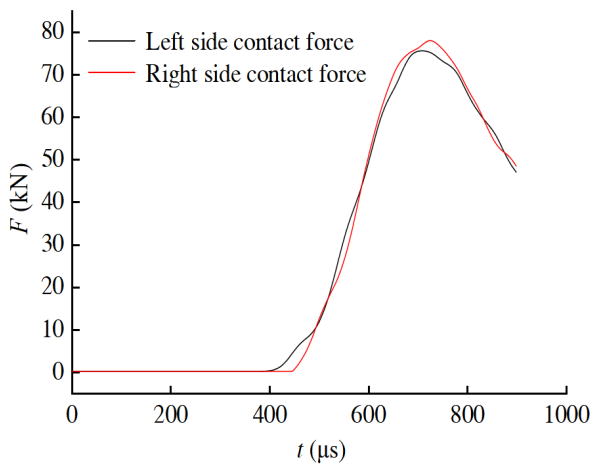


(a) Trapezoidal stress pulse with $t=200$ μs



(b) Trapezoidal stress pulse with $t=300$ μs



(c) Trapezoidal stress pulse with $t=400$ μs

**Fig. 8.** Contact forces on the left and right sides of the specimen with trapezoidal stress pulses.

As seen from Fig. 8, when the test being loaded with trapezoidal stress pulses of different lengths at 200 μs, 300 μs and 400 μs, as the stress waves propagate through the incident bar, specimen and transmission bar, the stress waves reach the left and right sides of the specimen one after another, and the contact forces on the left and right sides of the specimen are basically equilibrated and have the same trend, all showing a trend of first increasing and then decreasing with the propagation of the stress waves.

Being loaded with 200 μs, the contact forces on the left and right sides of the specimen oscillate significantly greater. Being loaded with 300 μs, the contact force oscillation between the left and right sides of the specimen is in second largest. Being loaded with 400 μs, the contact force oscillation between the left and right sides of the specimen is smaller. When the length of the loaded stress pulse is longer, the propagation of the axial stress wave in the bar is less affected by the transverse inertia effect. At this point, the contact force difference between the left and right sides of the specimen will also become small, and the degree of stress homogenization will be higher, resulting in a better dynamic equilibrium effect during loading.

As seen from Fig. 9, when triangular stress pulses of different time of 200 μs, 300 μs and 400 μs are loaded, the trend of contact force on the left and right sides of the specimen is basically the same as the trapezoidal stress pulses loaded, which also shows that when the length of stress pulses is larger, the smaller the oscillation trend of contact force on the left and right sides of the specimen, the better the dynamic loading balance effect.



(a) Triangular wave stress pulses with $t=200$ μs



(b) Triangular wave stress pulses with $t=300$ μs

(c) Triangular wave stress pulses with *t*=400 μs

**Fig. 9.** Contact forces on the left and right sides of the specimen with triangular stress pulses.

It can be seen from Figs. 8 and 9, as the trapezoidal stress pulse and triangular stress pulse being loaded, the NSCB specimen show that when the length of the stress pulse is larger, the transverse effect on the propagation of the stress wave is smaller. As the homogenization degree of stress of the specimen is in a higher stage, it is easy to achieve dynamic equilibrium. When trapezoidal stress pulse and triangular stress pulse of 400 μs are loaded, the contact forces on the left and right sides of the specimen match better, and both can achieve a better equilibrium. The trapezoidal stress pulse with 400 μs was chosen for further analysis.

**4.2 Trapezoidal stress pulses with different rise time**
The NSCB specimen is less affected by the transverse effect when the trapezoidal stress pulse is 400 μs. However, the rise times of the trapezoidal stress pulses vary for a given pulse length, and further analysis of the trapezoidal stress pulses with different rise times is required. This is to ensure that the transverse effect is minimized during dynamic loading.

The trapezoidal stress pulses of different rise times in Fig. 10 were loaded onto the end of the incidence bar to extract the contact forces on the left and right sides of the specimen and the axial stress waves at the same location on the incidence bar, as shown in Fig. 11.
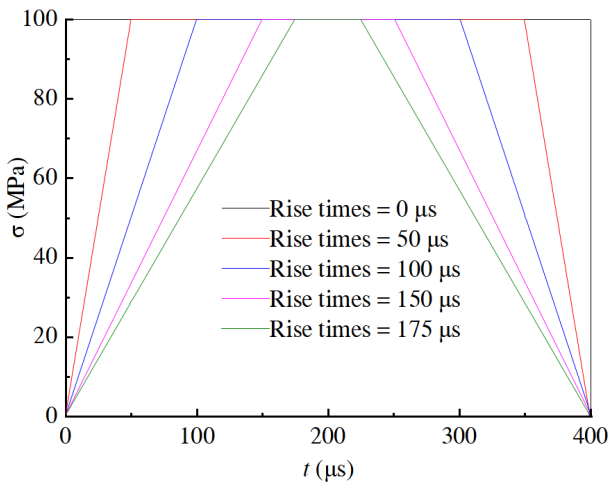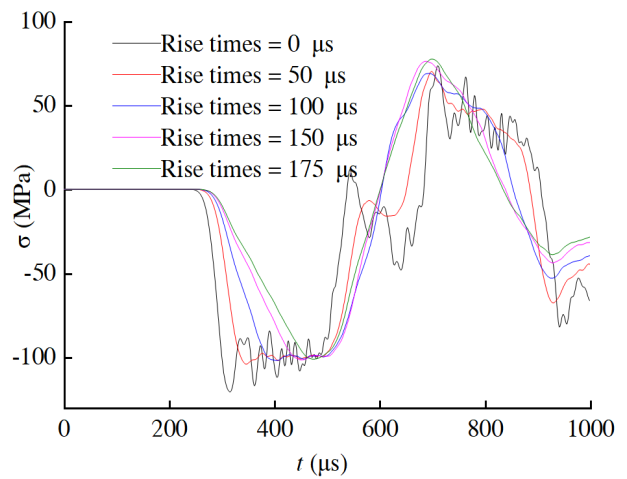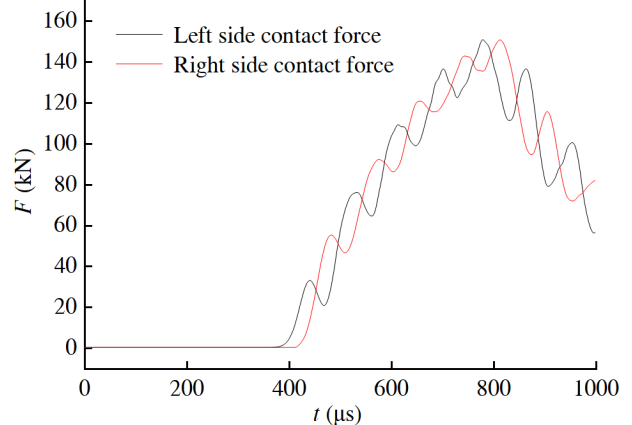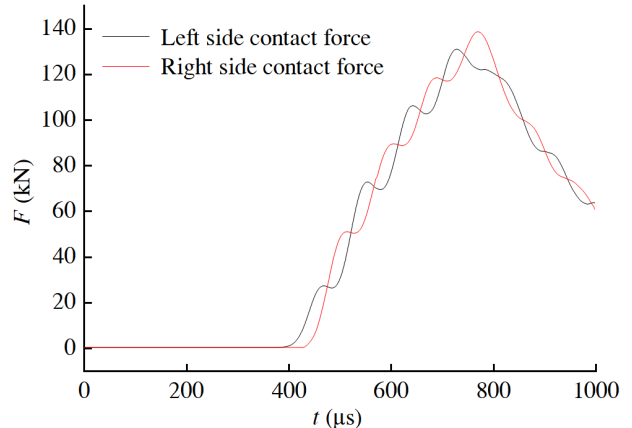


**Fig. 10.** Trapezoidal stress pulses with different rise time.
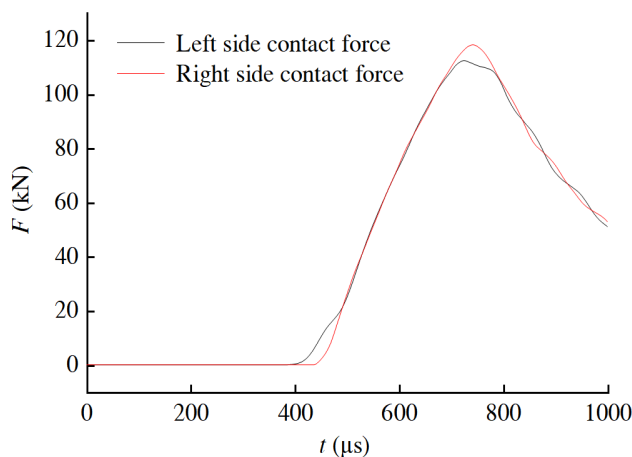


(a) The output of axial stress wave on the incident bar



(b) Contact forces with rise time of 0 μs



(c) Contact forces with rise time of 50 μs



(d) Contact forces with rise time of 100 μs

(e) Contact forces with rise time of 150 μs



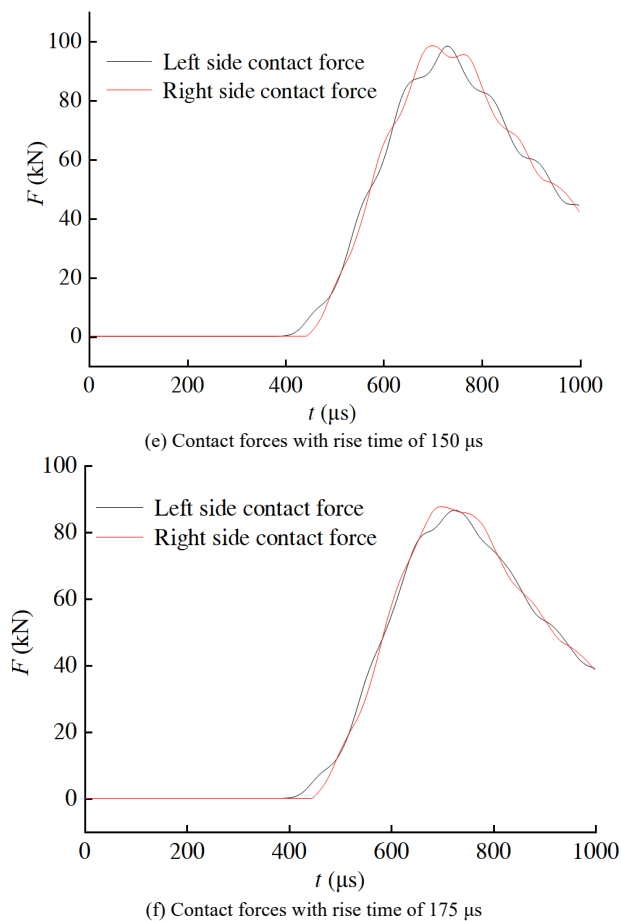(f) Contact forces with rise time of 175 μs

**Fig. 11.** Contact forces on the left and right sides of the specimen with different rise times and output axial stress on the incidence bar.

As seen from Fig. 11(a), when the trapezoidal stress pulse length is fixed, contact forces on the left and right sides of the specimen have the same trend when loaded with trapezoidal stress pulses of different rise time. With the rise time gradually increasing, the oscillation degree of contact force on the left and right sides first gradually decreases and then increases, and the curve fit gradually increases and then decreases. When the rise time is 100 μs, the oscillation of contact force on the left and right sides of the specimen was smaller and the curve fit was higher.

When loading with trapezoidal stress pulses of different rise times, the specimen stress homogenization gradually increases from high to low with the rise time increasing in a certain range, and the influence of the transverse effect gradually decreases and then increases. When the rise time is close to 1/4 of the trapezoidal stress pulse length, the influence of the transverse effect is small and the dynamic loading equilibrium is better.

As seen from the output of axial stress wave on the incident bar in Fig. 11(b), when the trapezoidal stress pulse of different rise times acts, the stress waveform extracted from the incident bar presents oscillation and dispersion phenomenon in the process of propagation as the rectangular wave with 0 μs rise time is loaded. Combined with the contact force on the left and right sides of the specimen at this time, the contact force also presents a larger oscillation phenomenon, indicating that the specimen is affected by the transverse effect and the equilibrium effect is poor. The incident wave is close to rectangular wave, which is similar to the rectangular wave obtained from the conventional Hopkinson impact test without pulse shaping technology and

special-shaped bullet impact, and also verifies the correctness of the numerical simulation in this paper.

When the rise time is 50 μs as shown in Fig. 11(c), the oscillation and dispersion of the stress waveform extracted from the incident bar decreases. When the rise time is 100 μs as shown in Fig. 11(d), the stress waveform dispersion is smaller. Combined with the contact force extracted from the left and right sides of the specimen at this time, the contact force also oscillates to a weak extent, and the two curves are in good agreement, which indicates that when the rise time is 100 μs, i.e. close to 1/4 of the trapezoidal stress pulse length, the specimen is least affected by the transverse effect and the equilibrium effect is better.

Due to the harmonic wave-speed of the Rayleigh approximation, the propagation speed of high frequency waves is lower and that of low frequency waves is higher. For linear elastic waves, the harmonic components of different frequencies have different phase velocities. The harmonic components in the rectangular stress pulse contain more high-frequency waves. The propagation velocity of the high-frequency components is lower than that of the low-frequency components, and the high-frequency components lag behind the wavefront, which result in the stress waves in the compression bar gradually dispersing during propagation, and the relative position of the wave-shape change, producing the phenomenon of wave dispersion. So, a symmetrical trapezoidal stress pulse loading with a pulse length of 400 μs and a rise time of 100 μs was selected for the NSCB specimens to ensure the accuracy of the finite element calculation.

### 4.4 Calculation of dynamic stress intensity factor

Based on the model of the SHPB loading system, the symmetrical trapezoidal stress pulse loading with a pulse length of 400 μs and a rise time of 100 μs was used to calculate the time-history curve of the dynamic SIF.

The contacted forces between the left and right sides of the specimen were averaged to obtain the average contact force $f$. The average contact force is brought into the aforementioned static Eq. (1) to calculate the time-history curve of the dynamic SIF. The calculation results are shown in Fig. 12(a). The results of the rectangular stress pulse with a pulse length of 400 μs and a rise time of 0 μs are presented in Fig. 12(b).
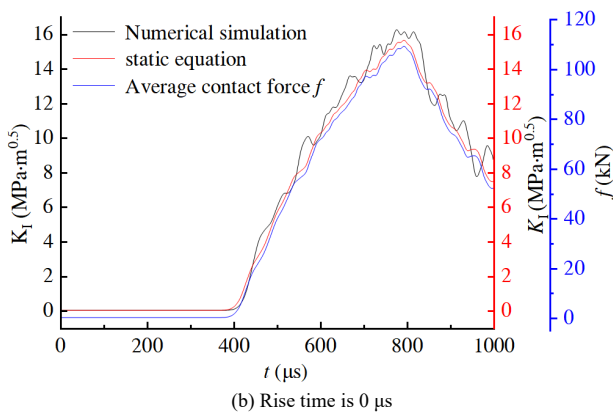


(a) Rise time is 100 μs
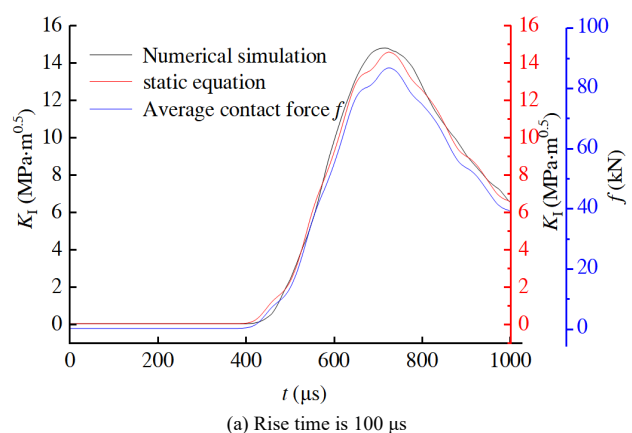
**Fig. 12.** Time-history curve of dynamic stress intensity factor with different rise times.

As seen from Figs. 12(a) and 12(b), comparing the loading results of a symmetrical trapezoidal pulse with a fixed pulse length of 400 μs and a rise time of 100 μs with those of a rectangular pulse with a rise time of 0 μs, the average contact force $f$ obtained by both of them has a similar trend. Both of them increase first and then decrease with the propagation of the stress wave. The dynamic SIF reaches its peak when the average contact force $f$ reaches the peak.

When the trapezoidal pulse loaded with a rise time of 100 μs compares with the rectangular pulse with a rise time of 0 μs, the former time-history curve of the dynamic SIF calculated by the numerical simulation is consistent with the static equation calculation results. The smaller the transverse inertia is, the smaller the stress difference between the two sides of the specimen is and the higher the degree of stress homogenization is during dynamic loading. when dynamic equilibrium is occurred, the static equation is used to calculate the dynamic SIF with a high degree of accuracy and a small error.

## 5. Conclusions

To study the dynamic SIF for fracture model I, the static and dynamic three-point bending numerical tests were carried out on NSCB specimens by using Abaqus software. The method of dimensional analysis was used to fit the $K$-factor formula of the fracture model I under static loading. Then this expression was extended to solve for the SIF under dynamic loading. The main conclusions are as following:

(1) The static SIF increases with the increase of relative crack length $a/R$ and ratio of the simple supported distance to the maximum diameter span $S/R$, and the stress intensity factor grows exponentially with $a/R$ and linearly with $S/R$. The increase of $S/R$ has a certain enhancement effect on the SIF at the crack tip.

(2) The loading trends of trapezoidal and triangular pulse on the realization of dynamic force equilibrium are similar. As the pulse length increases, the contact force oscillation on both sides of the specimen is reduced by the two pulses wave-shape, which has a weakening on the transverse inertia effect of dynamic loading.

(3) For the 400 μs trapezoidal stress pulse, the specimen is less affected by the transverse effect when the rise time is close to 1/4 of the total pulse time. The equation for the static SIF can be extended to solve for the dynamic SIF when the dynamic equilibrium is reached on both sides of the specimen.

This study has only carried out research in terms of numerical methods, and the applicability of the specific results needs to be verified experimentally. Only by combining numerical and experimental methods can the validity of equations obtained in this study be better verified.

---

**References**

1. Zhao, Y. H., Wang, S. R., Zou, Y. F., Wang, X. C., Huang, B. Q., Zhang, X. G., "Pressure-arching characteristics of fractured strata structure during shallow horizontal coal mining". *Tehnicki Vjesnik-Technical Gazette*, 25(5), 2018, pp. 1457-1466.
2. Wu, X., G., Wang, S. R., Yang, J. H., Zhao, J. Q., Chang, X. "Damage characteristics and constitutive model of lightweight shale ceramsite concrete under static-dynamic loading". *Engineering Fracture Mechanics*, 259, 2022, pp. ID 108137.
3. Zhao, Y. H., Wang, S. R., Zou, Z. S., Ge, L. L., Cui, F. "Instability characteristics of the cracked roof rock beam under shallow mining conditions". *International Journal of Mining Science and Technology*, 28(3), 2018, pp. 437-444.
4. Enderlein, M., Ricoeur, A., Kuna, M., "Finite element techniques for dynamic crack analysis in piezoelectrics". *International Journal of Fracture*, 131(3-4), 2005, pp. 191-208.
5. Aliha, M. R. M., Mahdavi, E., Ayatollahi, M., R., "The influence of specimen type on tensile fracture toughness of rock materials". *Pure and Applied Geophysics*, 174(3), 2017, pp. 1237-1253.
6. Cheng, L., Chang, X., Wang, S. R., Wang, Y., F., Zhang, M., X., "Effect analysis of bedding plane and fracture distribution on crack propagation process in layered fractured rock mass". *Journal of Engineering Science and Technology Review*, 14(5), 2021, pp. 90-99.
7. Luo, P. P., Wang, S. R., Hagan, P., Huang, Q. X., Cao, C., Gamage, K., "Influence of weak interlayer on mechanical performances of rock-like materials". *DYNA*, 94(4), 2019, pp. 447-454.
8. Wang S. R., Zhao J. Q., Wu X. G., Yang J. H., Liu A. "Meso-scale simulations of lightweight aggregate concrete under impact loading". *International Journal of Simulation Modelling*, 20(2), 2021, pp. 291-302.
9. Chang, X., Guo, T. F., Zhang, S., "Cracking behaviours of layered specimen with an interface crack in Brazilian tests". *Engineering Fracture Mechanics*, 228, 2020, pp. ID 106904.
10. Aliha, M. R. M., Ayatollahi, M. R., Smith, D. J., Pavier, M. J., "Geometry and size effects on fracture trajectory in a limestone rock under mixed mode loading". *Engineering Fracture Mechanics*, 77(11), 2010, pp. 2200-2212.
11. Franklin, J. A., Sun, Z., Atkinson, B. K., Meredith, P. G., Bobrov G. F., "Suggested methods for determining the fracture toughness of rock". *International Journal of Rock Mechanics & Mining Sciences & Geomechanics Abstracts*, 25(2), 1988, pp. 71-96.
12. Fowell, R. J., "Suggested method for determining mode I fracture toughness using cracked chevron notched Brazilian disc (CCNBD) specimens". *International Journal of Rock Mechanics and Mining Sciences & Geomechanics Abstracts*, 32(7), 1995, pp. 322.

13. Kuruppu, M. D., Obara, Y., Ayatollahi, M. R., "ISRM-suggested method for determining the mode I static fracture toughness using semi-circular bend specimen". *Rock Mechanics & Rock Engineering*, 47(1), 2014, pp. 267-274.
14. Aliha, M. R. M., Bahmani, A., "Rock fracture toughness study under mixed mode I/III loading". *Rock Mechanics & Rock Engineering*, 50(7), 2017, pp. 1-13.
15. Xing, Y., Huang, B., Ning, E., Zhang, L., Jin, F., "Quasi-static loading rate effects on fracture pProcess zone development of mixed-mode (I-II) fractures in rock-like materials". *Engineering Fracture Mechanics*, 240, 2020, pp. ID 107365.
16. Chong, K. P., Kuruppu, M. D., "New specimen for fracture toughness determination for rock and other materials". *International Journal of Fracture*, 26(2), 1984, pp. 59-62.
17. Mirsayar, M. M., Shi, X., Zollinger, D. G., "Evaluation of interfacial bond strength between Portland cement concrete and asphalt concrete layers using bi-material SCB test specimen". *Engineering Solid Mechanics*, 5(4), 2017, pp. 293-306.
18. Fayed, A. S., "Numerical evaluation of mode I/II SIF of quasi-brittle materials using cracked semi-circular bend specimen". *Engineering Solid Mechanics*, 2018, pp. 175-186.
19. Tang, S., Li, J., Zhang L, Liu, Z., Wang, S. Q., Dong, L. B., Wang, Z. Z., "Study on the static critical stress intensity factors of sandstone in a water environment based on semicircular bending specimens". *Theoretical and Applied Fracture Mechanics*, 116, 2021, pp. ID 103106.
20. Wang, Q. Z., Feng, F., Ni, M., Gou, X. P., "Measurement of mode I and mode II rock dynamic fracture toughness with cracked straight through flattened Brazilian disc impacted by split Hopkinson pressure bar". *Engineering Fracture Mechanics*, 78(12), 2011, pp. 2455-2469.
21. Wang, Q. Z., Yang, J. R., Zhang, C. G., Zhou, Y., Wu, L. Z., "Sequential determination of dynamic initiation and propagation toughness of rock using an experimental-numerical-analytical method". *Engineering Fracture Mechanics*, 141, 2015, pp. 78-94.
22. Wang, M., Zhu, Z., Dong, Y., Zhou, L., "Study of mixed-mode I/II fractures using single cleavage semicircle compression specimens under impacting loads". *Engineering Fracture Mechanics*, 177, 2017, pp. 33-44.
23. Wang, F., Zhu, Z., Wang, M., Qiu, H., Yin, P., "Investigation of mixed-mode I/II fracture under impact loading using split-hopkinson pressure bar". *Applied Sciences*, 10(20), 2020, pp. ID 7149.
24. Virgo, S., Abe, S., Urai J. L., "Extension fracture propagation in rocks with veins: Insight into the crack-seal process using discrete element method modeling". *Journal of Geophysical Research Solid Earth*, 118(10), 2013, pp. 5236-5251.
25. Ledit, R. F. A., Enrique, F., "The association between ambient air pollution and allergic rhinitis inception and control". *Current Treatment Options in Allergy*, 5(2), 2018, pp. 221-235.
26. Joudon, V., Portemont, G., Lauro, F., Bennani, B., "Experimental procedure to characterize the mode I dynamic fracture toughness of advanced epoxy resins". *Engineering Fracture Mechanics*, 126, 2014, 126, pp. 166-177.
27. Šraml, M., Kramberger, J., Dervarič, S., Glodež, S., "Fatigue behaviour of lotus-type porous structure: numerical approach". *Technical Journal*, 9(4), 2015, pp. 356-261.
28. Chen, W. N., Song, B., "*Split hopkinson (Kolsky) bar: design, testing and applications*". New York: Springer, USA, 2015, pp. 12-17.
29. Davies, R. M., "A critical study of the hopkinson pressure bar". *Series A, Mathematical and Physical Sciences*, 240(821), 1948, pp. 375-457.